

Postdeposition Sulfurization of CuInSe₂ Solar Absorbers by Employing Sacrificial CuInS₂ Precursor Layers

Faraz Khavari,* Nishant Saini, Jan Keller, Jes K. Larsen, Kostiantyn V. Sopiha, Natalia M. Martin, Tobias Törndahl, Charlotte Platzer Björkman, and Marika Edoff

Herein, a new route of sulfur grading in CuInSe₂ (CISe) thin-film solar absorbers by introducing an ultrathin (<50 nm) sacrificial sputtered CuInS₂ (CIS) layer on top of the CISe. Different CIS top layer compositions (Cu-poor to Cu-rich) are analyzed, before and after a high-temperature treatment in selenium (Se)- or selenium+sulfur (SeS)-rich atmospheres. An [S]/([S] + [Se]) grading from the surface into the bulk of the Se- and SeS-treated samples is observed, and evidence of the formation of a mixed CuIn(S,Se)₂ phase by Raman analysis and X-ray diffraction is provided. The optical bandgap from quantum efficiency measurements of solar cells is increased from 1.00 eV for the CISe reference to 1.14 and 1.30 eV for the Se- and SeS-treated bilayer samples, respectively. A ≈ 150 mV higher V_{OC} is observed for the SeS-treated bilayer sample, but the cell exhibits blocking characteristics resulting in lower efficiency as compared with the CISe reference. This blocking is attributed to an internal electron barrier at the interface to the sulfur-rich surface layer. The difference in reaction routes and possible ways to improve the developed sulfurization process are discussed.

1. Introduction


S alloying in Cu(In,Ga)Se₂ (CIGSe) leads to an upshift of the conduction band minimum in combination with a downshift of the valence band maximum.^[1,2] This contrasts to Ga alloying, which almost exclusively leads to an upshift of the conduction band. In order to avoid possible minority carrier blocking effects, it may be more beneficial to use sulfur grading at the interface and gallium grading in the bulk and at the back contact of the absorber. Indeed, sulfur incorporation in the form of sulfurization has proven successful to reduce interface recombination in

chalcopyrite solar cells. This sulfurization can be used in combination with gallium grading to further improve the performance of CIGSe-based thin-film solar cells.^[3–5] Additionally, postdeposition sulfurization is suggested to passivate deep trap states,^[6] increase electron lifetime,^[7] and improve hole mobility.^[8] In the sequential process, adding sulfur at the end of the annealing step enables Cu(In,Ga)(S,Se)₂ (CIGS_{Se}) alloy formation at the absorber surface. This process is referred to as annealing of stacked-elemental layers in S-containing atmosphere^[7] or sulfurization-after-selenization.^[9] A world record efficiency of 23.35% for CIGS_{Se} has been achieved through the latter approach using toxic hydrogen sulfide (H₂S) gas as the S source.^[9] For the purpose of avoiding toxic H₂S, several studies performed sulfurization of coevaporated absorbers in elemental sulfur atmosphere with the

intention of similar device improvement.^[5,10–15] However, this approach led to the formation of a pure CuInS₂ (CIS) layer on top of Cu-depleted CIGSe with a Ga pile-up near the CIGS_{Se}/CIS interface. This approach resulted in a reduced fill factor (FF) and blocking behavior, presumable caused by the wide-gap Ga-rich CIGSe near the interface.^[13,16] While the CIS layer provides a higher surface bandgap and, thereby, increases open-circuit voltage (V_{OC}),^[13] the conversion efficiency was not increased, possibly due to the formation of an electron barrier at the CIGSe/CIS interface. For the CIGSe absorbers with Ga-free surfaces, a much higher in V_{OC} , FF, and efficiency was observed after sulfurization^[5,14] although short-circuit current density (J_{SC}) was always lower. The lower J_{SC} after sulfurization has been attributed to: 1) emergence of an electron barrier at the CuInS₂/CuIn(S,Se)₂ interface, 2) shrinkage of the space-charge region width due to higher doping in the newly formed CuInS₂, or 3) enhanced recombination at the grain boundaries (GBs) owing to the higher S concentration therein. In our recent study of Cu-poor CuInSe₂ (CISe),^[15] we confirmed that a 180 nm-thick conformal surface CIS layer is formed after absorber sulfurization at 530 °C, decreasing both FF and J_{SC} . At the same time, we found that these adverse effects can be alleviated by lowering the treatment temperature to 430 °C, at which an inhomogeneous surface CuIn(S,Se)₂ (CIS_{Se}) alloy is produced instead. These results indicate that further efficiency gains are possible with a better control over S incorporation from the elemental source.

Our previous findings also indicate that the form of S incorporation depends on the off-stoichiometry of CISe. This is

F. Khavari, N. Saini, J. Keller, J. K. Larsen, K. V. Sopiha, N. M. Martin, T. Törndahl, C. P. Björkman, M. Edoff
 Solar Cell Technology
 Department of Materials Science and Engineering
 Uppsala University
 Box 534, Uppsala SE-75103, Sweden
 E-mail: Faraz.khavari@angstrom.uu.se

 The ORCID identification number(s) for the author(s) of this article can be found under <https://doi.org/10.1002/pssa.202100441>.

© 2021 The Authors. physica status solidi (a) applications and materials science published by Wiley-VCH GmbH. This is an open access article under the terms of the Creative Commons Attribution-NonCommercial-NoDerivs License, which permits use and distribution in any medium, provided the original work is properly cited, the use is non-commercial and no modifications or adaptations are made.

DOI: 10.1002/pssa.202100441

because CIS is inherently less tolerant to Cu deficiency, and thus it always forms with the perfect $[\text{Cu}]/[\text{In}] = 1$ ratio, which is achieved by extracting Cu from the CISE layer underneath. As a result, for a better SSSE profile, the approach suggested in this study is to use a sacrificial sputtered precursor layer of CIS followed by a fast anneal in a sulfur and/or selenium-containing atmosphere to react the CIS layer with the underlying CISE absorber. By adding copper and sulfur simultaneously, we anticipated that issues related to reorganization of the absorber upon sulfurization with elemental sulfur or elemental sulfur and selenium could be avoided.

Therefore, in this study, bilayers of bulk CISE with an absorber composition of $[\text{Cu}]/[\text{In}] = 0.85 \pm 0.5$ with three different CIS top layer compositions of $[\text{Cu}]/[\text{In}] = 0.6$ (Cu-poor), 0.9 (near-stoichiometric), and 1.4 (Cu-rich) are exposed to vaporized elemental selenium (Se) or selenium with sulfur (Se + S) atmospheres with the objective to: 1) form SSSE grading limited to the surface region of the absorber layer, 2) investigate the effect of surface composition on CISSE formation, 3) examine the role of the sputter-deposited CIS interfacial layer of the untreated bilayers (CISE/CIS-Un) in the Se or (Se + S) incorporation into the absorber layer, and 4) investigate the impact of the sacrificial layer on the device behavior.

2. Experimental Section

2.1. Sample Preparation

All solar cells in this study were produced in the form of sequential stacks of soda lime glass (SLG)/Mo/NaF/absorber/CdS/i-ZnO/ZnO:Al as pictured in **Figure 1**. Prior to absorber deposition, a 350 nm molybdenum layer was deposited on 3 mm SLG substrates using DC magnetron sputtering, followed by a ≈ 10 nm sodium fluoride (NaF) layer added via thermal evaporation from an effusion source. Two $5 \times 5 \text{ cm}^2$ samples were produced in each absorber run. The CuInSe_2 (CISE) layer was coevaporated in a high vacuum deposition system, following a

three-stage (Cu-poor \rightarrow Cu-rich \rightarrow Cu-poor) process with constant rates for In and Se. During the evaporation, the substrate temperature was increased from 450 to 550 °C. Mass spectrometer and temperature control were used for the metal deposition rates and selenium control, respectively. The $[\text{Cu}]/[\text{In}]$ ratio of the fabricated CISE absorbers varied from 0.8 to 0.9, as extracted from X-ray fluorescence (XRF) measurements calibrated with a standard CIGSe sample of known composition. The thickness of the coevaporated CISE absorbers was in the range of 1.2–1.3 μm , as determined from scanning electron microscopy (SEM) analysis (see Figure S1, Supporting Information). All the samples were protected from surface oxidation with a thin CdS capping layer (≈ 50 nm), which was added by chemical bath deposition within 5 min after unloading the CISE absorbers from the coevaporation system. The samples were subsequently divided into four $2.5 \times 2.5 \text{ cm}^2$ pieces: three for sputtering of a thin layer of CIS (making CISE/CIS bilayers) (see next paragraph), and one as a CISE reference (see Figure 1). Among the three bilayer samples, one was annealed in elemental selenium (Se-sample) and one in selenium + sulfur atmosphere (SeS-sample) (see Section 2.3), whereas the last one was left untreated (Un-sample), see Figure 1.

2.2. Cu–In–S sputtering

Prior to the sputtering of CIS layer (≈ 50 nm), the CdS capping layer was removed from the surface of the CISE by etching in a solution of 2 M HCl for 60 s. The resulting samples were immediately transferred into the sputtering system with the use of a load lock. The base pressure of the sputtering chamber was below 10^{-6} Torr and the sputtering was performed at 4 mTorr of Ar flowing at 50 sccm. The CIS layer was deposited by cosputtering from 3 in. indium sulfide (In_2S_3) and copper sulfide (CuS) targets (In_2S_3 : RF magnetron sputtering at 1.75 W cm^{-2} and CuS: pulsed DC magnetron sputtering at 0.85 W cm^{-2}), while no heating was applied to the substrate holder. The sputtering time was 400 s. In order to obtain a CIS layer with uniform composition, the substrate holder was rotated at 20 rotations per

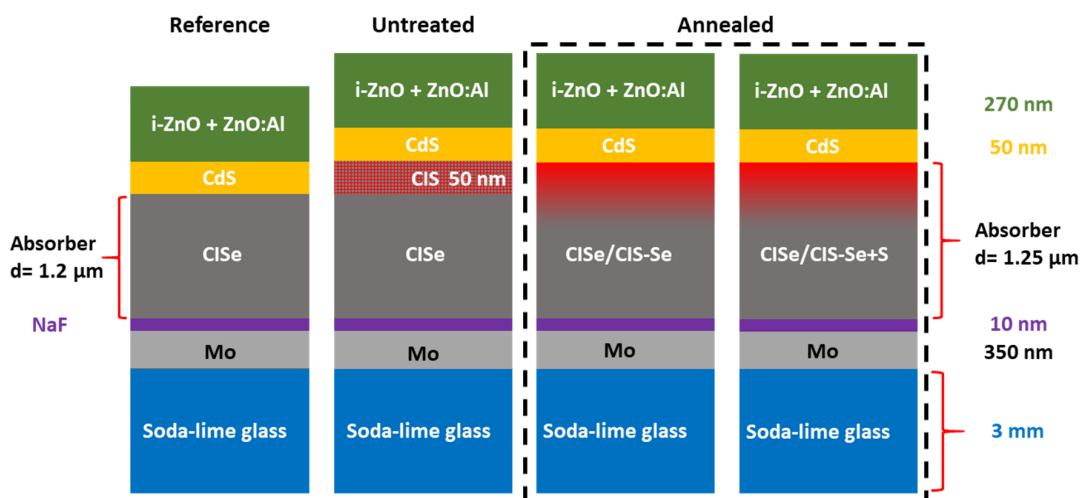


Figure 1. Schematic of a full stack processing of a CISE solar cell. Each sample is divided into four pieces after the CISE deposition: one used as a reference (first column), one with a thin sputtered CIS layer to create the untreated CISE/CIS bilayer (second column), and the other two for the additional selenization (third column) or selenization + sulfurization (fourth column).

minute (rpm). The elemental composition and thickness of the cosputtered CIS layer were controlled by the applied power to the aforementioned targets and by the sputtering time, respectively. The [Cu]/[In] ratio of the sputtered CIS layers was varied between 0.6, 0.9, and 1.4 as estimated from the subsequent XRF measurements of a monitoring sample, which was placed in the center of the substrate holder. To protect the samples from oxidation, the fabricated specimens were redeposited with CdS until further treatments were implemented (see next paragraph).

2.3. Selenium and Selenium + Sulfur Incorporation into the CISE/CIS Bilayer Structure

Before the annealing in elemental Se or Se + S atmosphere, the CdS capping layer was once again removed by etching, as described in Section 2.2. Then, the bilayer samples were transferred into a custom-built annealing chamber using a small graphite transfer box. After preheating the sublimation source chamber, 700 mg of elemental Se for the treatment in pure Se or 350 mg of Se + 350 mg of S for the Se + S treatment was introduced into the chamber, which then vaporized immediately. Next, at the estimated sample temperature of 530 °C, during 60 s, the Se or Se + S gas mixtures were brought into the reactor with a flow of Ar carrier gas. The annealing process in Se or in Se + S lasted for 10 min, which was followed by a cooling down step of 30 min in Ar atmosphere. The CdS layer was again redeposited within 5 min after extracting the samples from the annealing system. Further details of the annealing process and the setup can be found in refs. [13,15].

2.4. Solar Cell Fabrication

The absorber deposition process and pn junction formation have been described in Section 2.2. Further details on the CdS deposition procedure can be found elsewhere.^[13,15] To finish the cells, a window layer stack of intrinsic ZnO and aluminum-doped ZnO (i-ZnO + ZnO:Al) with the total thickness of 270 nm and sheet resistance of 45 $\Omega \text{ sq}^{-1}$ was deposited on all pieces by RF magnetron sputtering. Finally, 15 individual cells with an area of 0.05 cm² were defined for each sample by mechanical scribing.

2.5. Material and Device Characterization

Raman spectroscopy was carried out in a Renishaw inVia system to investigate the sulfur incorporation and the resulting phase compositions at the absorber surfaces. As the excitation source, a green laser of 532 nm wavelengths with an estimated probing depth of 200 nm was used. The analysis was performed during 40 s at 50 \times magnification, where the numerical aperture was 0.75 and the estimated power density was 5000 W cm⁻². The crystallinity and phase compositions in the bulk and close to the surface were confirmed by performing θ -2 θ and grazing incidence-XRD (GI-XRD) scans in a Philips X'pert MRDII system. In GI-XRD, different incident angles were used (0.5° and 1.0°), which allowed probing the entire film thickness, but with emphasis on different depths of the sample. To better understand the surface chemistry, X-ray photoelectron spectroscopy (XPS) measurements were performed using a PHI Quantera II scanning XPS

microprobe with monochromatized Al K α (1486.6 eV) and a beam diameter of 100 μm . The base pressure in the analysis chamber was about 10⁻⁹ mbar during the XPS measurements. Pass energies of 224 and 55 eV with dwell times of 0.05 s/point were used to collect the survey and detailed spectra, respectively. The samples were loaded into the spectrometer shortly after etching away the CdS capping layer and rinsing the bare absorber with water. To investigate the absorber topology and the solar cell cross section, SEM analysis was performed in a Zeiss 1550 system with an acceleration voltage of 5 kV. Transmission electron microscopy and energy dispersive X-ray spectroscopy (TEM-EDS) were employed for further cross-sectional imaging and elemental mapping. For this purpose, FEI-Titan Themis 200 was operated at an acceleration voltage of 200 kV. The TEM lamellae were prepared using focused ion beam (FIB). More details about the sample preparation with FIB can be found in our earlier studies.^[5,13-15] In addition, compositional depth profiles were obtained with glow discharge optical emission spectroscopy (GDOES) using a Spectrums Analytik GmbH GDA 750 instrument with the sputtering crater of 4 mm in diameter.

The electrical parameters of the completed solar cells were characterized using a home-built external quantum efficiency (EQE) and current-voltage (J - V) measurement setups. The EQE data were collected under a Xe arc lamp. The calculated J_{sc} extracted from the EQE and AM1.5 G standard spectrum was used to calibrate the J - V measurements. The J - V analysis was conducted at room temperature (25 °C) using a ELH lamp calibrated with a Si reference to a photon flux intensity corresponding to AM1.5 G at 100 mW cm⁻².

3. Results and Discussion

3.1. Characterization of the Absorber Films

3.1.1. Raman Spectroscopy

Raman spectra of the CISE reference samples and of the CISE/CIS bilayered absorbers before and after Se or Se + S treatments are shown in **Figure 2**. The corresponding spectra but in a broader range of wavenumbers and grouped by the treatment are presented in Figure S2, Supporting Information. As can be seen, all CISE references have similar Raman spectra with the dominant A₁-Se-Se peak at 174 cm⁻¹. The main difference is the intensity of the ordered vacancy compound (OVC) peak at 156 cm⁻¹, which, as expected, is higher for the most Cu-poor composition (see Figure S2a, Supporting Information).

The Raman spectra of the untreated CISE/CIS bilayers are less similar (follow the red curves in Figure 2) due to the greater variation in [Cu]/[In] for the CIS top layer. Here, the signal from A₁-Se-Se vibrations in CISE is still dominant but an additional peak at 290 cm⁻¹ corresponding to the A₁-S-S vibration in CuIn(S,Se)₂ emerges for all three samples. In addition, a broad peak with the intensity correlating with the [Cu]/[In] ratio in the top CIS layer appears at \approx 475 cm⁻¹ (see Figure S2b, Supporting Information). This Raman shift can be ascribed to Cu_{2-x}S, which segregates in Cu-rich films. The observation of this peak in the untreated 0.9 sample, which is not supposed to be Cu-rich, may indicate that the CIS composition is not 0.9 but closer to

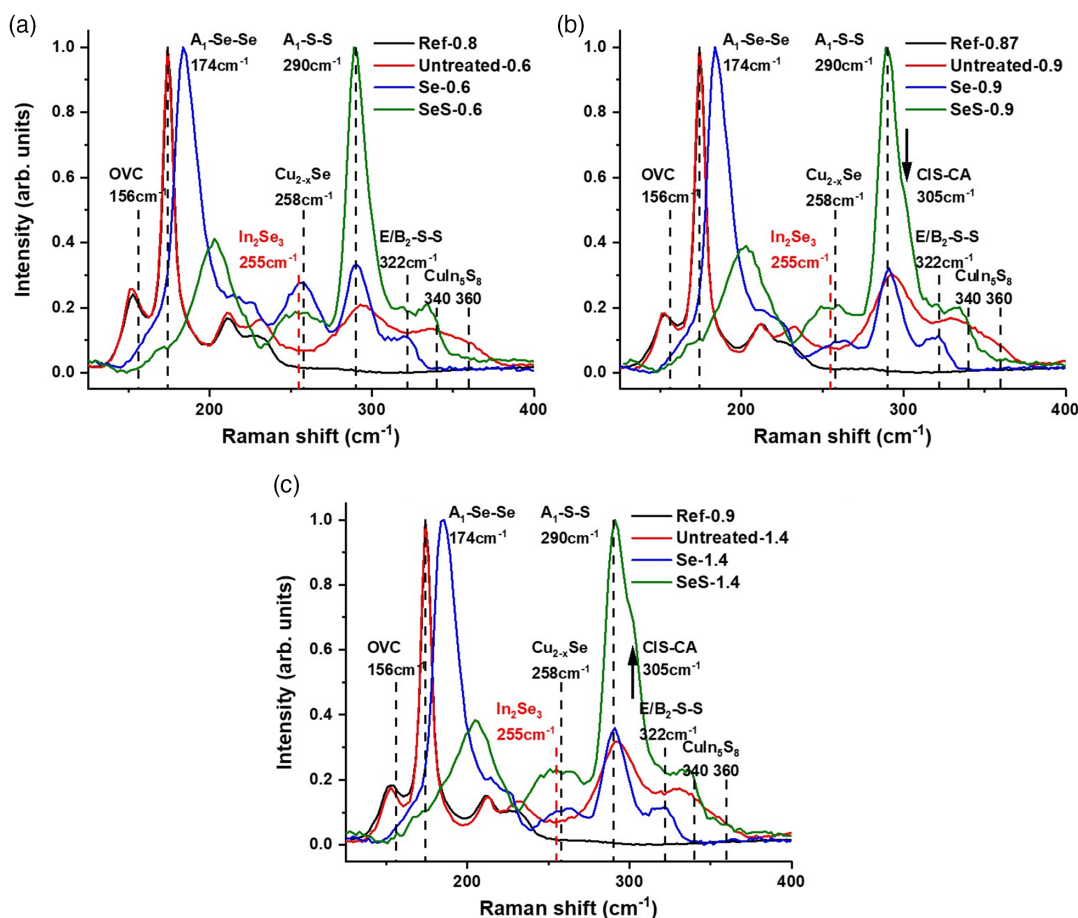


Figure 2. Normalized Raman spectra of the CISE/CIS bilayers with different compositions of the CIS top layer, $[Cu]/[In] = a$ 0.6, b) 0.9, and c) 1.4. The following color code has been used: untreated (red) and after treatment with Se (blue) or Se + S (green). For a better comparison, the corresponding CISE references are included (black). The dashed lines indicate the Raman shifts corresponding to different phases reported elsewhere.^[17,19,22,23,45]

1.0. The peak may be shifted towards lower wavenumbers if $Cu_{2-x}S$ has $x > 1$.^[17,18] The E/B_2 peak of the S-S longitudinal optical (LO) phonon vibration at 322 cm^{-1} is more asymmetric toward the higher wavenumbers (around 360 cm^{-1}) for the untreated-0.6 sample with the most Cu poor top layer. This feature can be explained by the presence of a spinel $CuIn_5S_8$ phase that has been detected in similar sputtered materials before.^[19] However, a contribution from In_2S_3 cannot be excluded.^[20,21] The spinel $CuIn_5S_8$ (or In_2S_3) phase is not observed in the samples treated with Se, which means that this compound has been transformed into other phases. A possible route is that it was consumed by supplying S (and Cu) into the CISE layer underneath, while the remaining In reacted with Se from the annealing atmosphere (or with Se expelled from CISE upon S incorporation). The $A_1\text{-Se-Se}$ peaks are broadened and slightly shifted toward higher wavenumbers as compared with the references and untreated bilayer samples (follow the blue curves). This behavior indicates the formation of a Se-rich $CuIn(S,Se)_2$ alloy.^[22] At the same time, the $A_1\text{-S-S}$ peak remains at $\approx 290\text{ cm}^{-1}$, suggesting that the $CuInS_2$ phase remains almost free of Se. The peak at 475 cm^{-1} disappears after the treatment, signifying that the $Cu_{2-x}S$ phase detected in Cu-rich CIS layers has been fully incorporated into the absorber

(see Figure S2c, Supporting Information). The OVC peak at 156 cm^{-1} for Cu-poor CISE layers also vanishes, presumably due to the formation of a more conformal CIS coverage. Instead, two additional peaks appear around 255 and 490 cm^{-1} (see the broader range of wavenumbers in Figure S2, Supporting Information). These two vibrations are reported to be associated with In_2Se_3 ,^[23] which explains why they are the strongest for the most Cu-poor CIS layer (Se-0.6). Note that the peak at 255 cm^{-1} may overlap with the $Cu_{2-x}Se$ phase at 258 cm^{-1} , which usually forms in the near-stoichiometric or Cu-rich CISE absorbers, but we do not expect it to occur in these samples. To further investigate the possible existence of an indium-rich phase at the surface, XPS analysis was carried out (see Figure S3–S5, Supporting Information, and the supporting text).

When the untreated bilayers are subjected to Se + S (follow the green curve), the $A_1\text{-S-S}$ vibration peak becomes dominant owing to the larger CIS volume fraction grown under the additional S supply from the elemental gas. The peak position matches that of the pristine chalcopyrite CIS compound (CH-CIS, space group $I-42d$ ^[24]), meaning that Se incorporation into the surface CIS is negligible. However, a clear shoulder appears at the side of higher wavenumbers of the $A_1\text{-S-S}$ peak (at $\approx 305\text{ cm}^{-1}$) for the SeS-0.9

and SeS-1.4 samples (pointed by the arrow in Figure 2b,c and see Figure S2d, Supporting Information). This feature has neither been seen in sulfurized films in our previous works^[13,15] nor in a similar study,^[22] but it can be explained by the presence of CIS with CuAu-type ordering (CIS-CA, space group $P-4m2$ ^[24,25]) observed in stand-alone sputtered CIS films before.^[26] Further, as compared with the sample annealed in Se, both the shift and the broadening of the A_1 -Se-Se peak are more pronounced after Se + S treatment, reflecting higher SSSe ratio in the Se-rich CuIn(S,Se)₂ alloy. This observation is also consistent with the additional S supply from the Se + S atmosphere.

3.1.2. X-Ray Diffraction

XRD in θ - 2θ and grazing incidence mode (GI-XRD) can be used to assess the phases both at the surface and in the bulk. It is

complementary to Raman and XPS as it detects diffracting planes in crystalline phases rather than the chemical environment. Furthermore, GI-XRD is much more surface sensitive compared with θ - 2θ . The results of XRD analysis for the untreated and treated samples with Se and Se + S are illustrated in Figure 3. From θ - 2θ scans of the reference samples in Figure 3a–c, a sharp CISe (112) characteristic peak appears at 26.6° . For the untreated sample, the second peak arises at $\approx 27.8^\circ$, which agrees well with the position of the CIS (112) peak (see GI-XRD), while the CISe signal remains unaffected. This behavior suggests that the crystal structure of the underlying CISe absorber did not change during sputtering of the top CIS layer. After Se and Se + S treatments, the (112) peak is slightly broadened and shifted to higher 2θ angles, which is in agreement with the broadening of the A_1 -Se-Se peak in the Raman analysis. This systematic shift indicates alloy formation of CuIn(S,Se)₂ not only at the surface region but also deeper

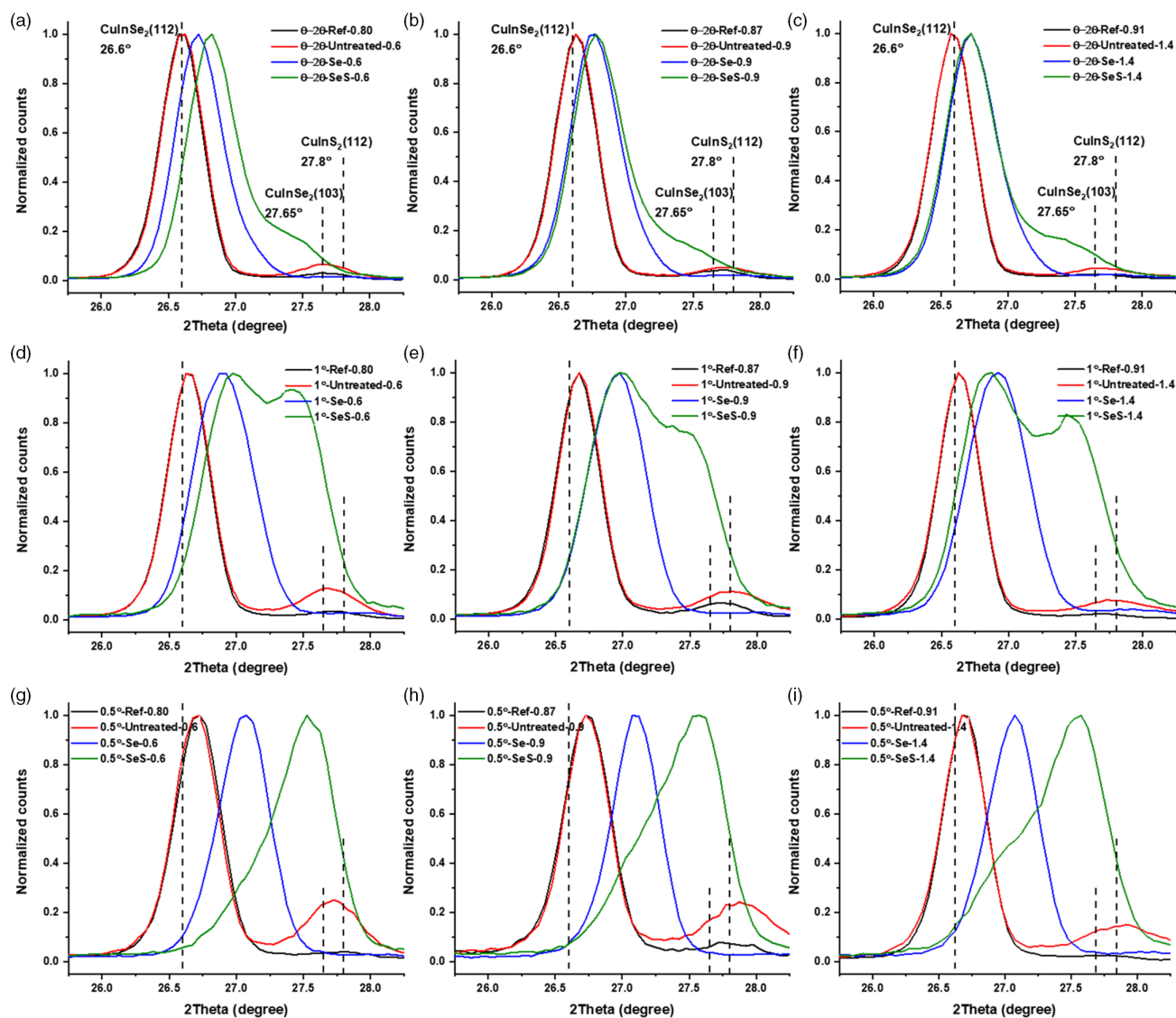


Figure 3. XRD analysis of the selenized (blue) and sulfurized+selenized (green) CISe/CIS bilayers compared with the corresponding untreated (red) and reference (black) samples. a–c) θ - 2θ scans, d–f) and g–i) GI-XRD scans at incidence angle (α) = 1° and 0.5° , respectively.

in the absorber. It should be noted that the peak shift is less for the selenized sample than for the Se + S-treated sample. However, for the Se + S-treated samples a clear tail appears at higher 2θ angles, overlapping with the CISe (103) peak at 27.65° . In order to intensify the signal from the near-surface regions, GI-XRD analysis was performed at grazing incidence angles of $\alpha = 1^\circ$ and 0.5° . For the selenized sample in Figure 3g–i (blue curve), the symmetry of the (112) peak does not significantly change, but slightly broadens as the incidence angle (α) is increased from 0.5° to 1° in Figure 3d–f. This indicates that a $\text{CuIn}(\text{S},\text{Se})_2$ alloy is formed with a low and declining S content from the surface into the bulk. Unlike for the selenized samples, at $\alpha = 0.5^\circ$, a pronounced shoulder appears at lower 2θ angles for the Se + S-treated samples (SeS), which evolves into a distinct peak for $\alpha = 1^\circ$. This dependence on the incidence angle can be interpreted as the formation of two $\text{CuIn}(\text{S},\text{Se})_2$ alloys with different SSSe ratios.

3.1.3. GDOES Profiling

GDOES adds yet another perspective to the material analysis. This method is well-suited for the assessment of elemental depth distributions, but it is less accurate close to surfaces and interfaces. The measured GDOES elemental depth profiles for the samples with CIS surface of $[\text{Cu}]/[\text{In}] = 0.6$ are illustrated in Figure 4. It should be noted that the $[\text{Cu}]/[\text{In}]$ ratio has almost no effect on these profiles (see Figure S6, Supporting Information). As a guide to the eye, the onset of the molybdenum signal (90% of full intensity) for the reference sample is marked with a vertical line. As one can see, smooth SSSe gradients are formed from the surface into the bulk after both Se and Se + S treatments, with the SSSe ratio being significantly lower at the surface of the Se-treated sample. This is consistent with the higher S content in the Se + S-treated samples measured with Raman above and XPS (Figure S4, Supporting Information).

The shallow SSSe variation of the Se-treated sample agrees with the formation of $\text{CuIn}(\text{S},\text{Se})_2$ with a low and declining S content from the surface toward the bulk, which is in line with the observed single peak in GI-XRD analysis of the Se-treated sample. A significant sulfur pile-up is measured near the absorber/Mo interface, which indicates the formation of either MoS_2 or $\text{Mo}(\text{S},\text{Se})_2$.^[27,28] In agreement with the XRD analysis, the formation of a SSSe grading seems to be independent of

the $[\text{Cu}]/[\text{In}]$ ratio of the as-deposited sulfide layer, as seen in Figure S6, Supporting Information. This observation agrees with earlier studies, where we concluded that Cu transport to the reaction fronts takes place via Cu vacancies,^[5] since Cu-depletion is observed even for the sample with the $[\text{Cu}]/[\text{In}] = 1.4$.

On the other hand, using an additional external elemental sulfur source (Se + S) increased S incorporation into the absorber. Also, the $\text{Mo}(\text{S},\text{Se})_2$ signal is more pronounced for all SeS samples. Similar to the selenized samples, a nonuniform $\text{CuIn}(\text{S},\text{Se})_2$ alloy is formed for the SeS samples, but with a greater S concentration close to the surface (SSSe = 0.8), as shown in Figure S4–S6, Supporting Information. This result differs from studies previously carried out when only sulfur was available in the atmosphere^[15] resulting in a pure CuInS_2 layer (SSSe = 1) at the surface. The results from the sample with the lowest $[\text{Cu}]/[\text{In}]$ ratio are slightly different from the less Cu-poor samples with the sulfur profile extending further into the absorber layer. This is in line with the indicated peak shift observed with XRD for this sample. The high surface sulfur concentration also agrees with the GI-XRD results where two distinguished peaks were observed when the incidence angle decreased from 1° to 0.5° (see Figure 3). Moreover, the GDOES results of the treated samples indicate a long-range redistribution of copper (Cu enrichment) in regions of S incorporation. This behavior is necessary to form $\text{CuIn}(\text{S},\text{Se})_2$ alloy, requiring near-stoichiometry of $[\text{Cu}]/[\text{In}] \approx 1$ ^[29] (see Figure S7, Supported Information), in particular as CA may allow Cu-deficiency.

3.1.4. STEM-EDS Characterization

The STEM-EDS cross-section images of the untreated-0.6 sample before and after annealing in Se + S atmosphere are shown in Figure 5. Before annealing, the sputtered CuInS_2 forms a conformal layer with an average thickness of about 40–50 nm. This thin CIS layer is found to be nanocrystalline. A magnified STEM image of a region close to the heterojunction is illustrated in Figure S8, Supporting Information. The EDS elemental map of the untreated sample indicates a homogeneous absorber with no sign of secondary phases (see wider lamella view in Figure S9, Supporting Information). After annealing in Se + S atmosphere, a crystalline layer is formed at the surface and a region with voids appears at the back contact. SEM analysis confirms that these voids are formed in all compositions (see Figure S1,

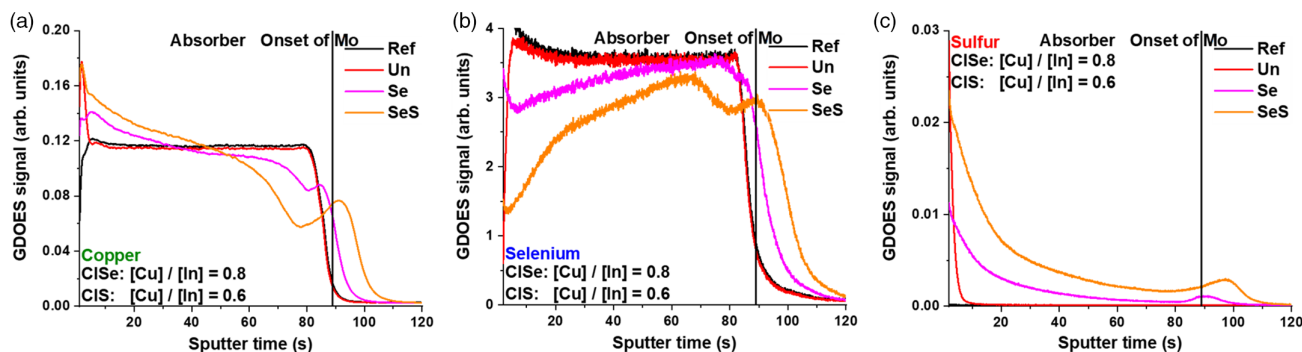


Figure 4. GDOES elemental depth profiles of a) Cu, b) Se, and c) S in the bilayers with $[\text{Cu}]/[\text{In}] = 0.6$ in the CIS layer before and after treatment in Se and Se + S atmosphere. The CISe reference is also given for comparison. The capping CdS layer was removed before the measurement.

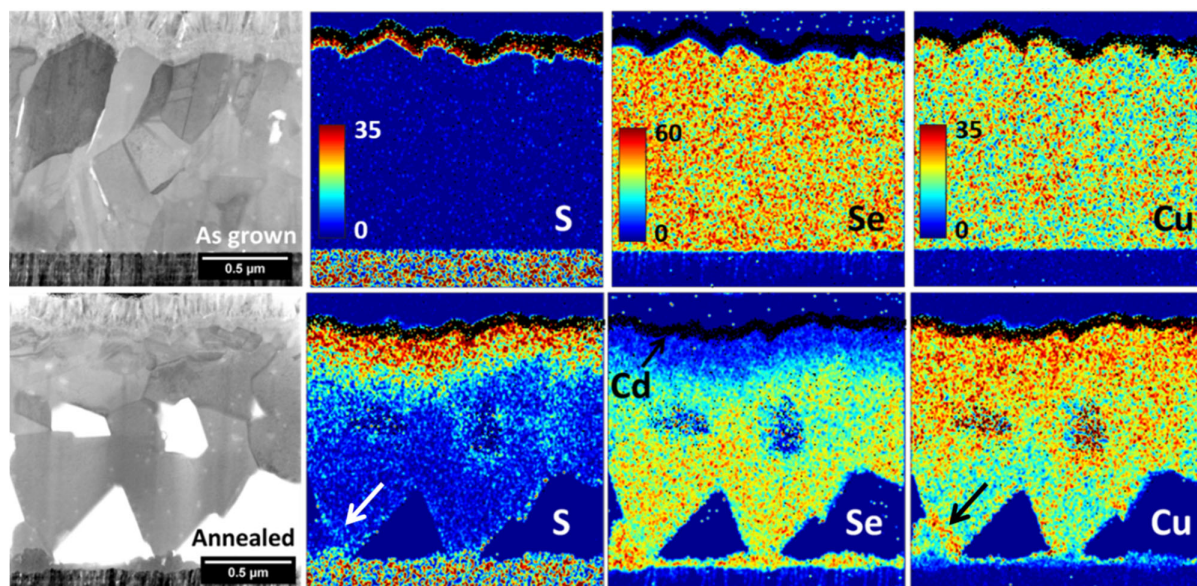


Figure 5. STEM-EDS cross-sectional imaging of untreated-0.6 (top row) and SeS-0.6 (bottom row) samples (full stack solar cells). The color bars give the respective elemental concentrations in at.% and the CdS is illustrated by black pixels in each map.

Supporting Information) as a result of the harsh annealing process in Se + S atmosphere at 530 °C. Sulfur is observed at the surface, in the bulk, and at the back in the STEM-EDS map. For the grains formed at the surface, it seems that sulfur reaches a plateau value (see Figure S8b, Supporting Information) with an SSSe ratio of about 0.8. Below this region, the S concentration strongly decreases toward the Mo/CISe interface, where Mo(S,Se)₂ layer grows with a thickness that varies laterally (See Figures S8b and S10b, Supporting Information). Furthermore, the Cu concentration increases in regions of S incorporation, which confirms that Cu stoichiometry ($[Cu]/[In] \approx 1$) is required to form a CuIn(S,Se)₂ alloy. The Cu enrichment close to the surface is stronger for the Se + S treated than for the selenized sample confirmed from GDOES. Therefore, copper is intensely depleted from the back region of the SeS-0.6 sample. Nevertheless, close to the Mo(S,Se)₂ layer, in the lowest left grain boundary (indicated by arrows in Figure 5), there is S enrichment, which comes with a Cu enrichment (can also be found in Mo(S,Se)₂ layer). These observations agree with the GDOES results (see Section 3.1.3). The Cu in-diffusion together with the S reaction may be explained by S diffusion from the surface toward the back, thereby taking Cu with it. Since K α spectral lines of sulfur and molybdenum nearly overlap, the S concentration in the Mo layer cannot be quantified with EDS. However, the GDOES results have shown that there is S in the MoSe₂. Moreover, the $[Cu]/[In]$ is slightly higher at the surface of the selenized samples than the Se + S. The In enrichment at the front surface together with S and Na (see Figure S11, Supporting Information) may originate from NaInS₂.^[5,30] This phase may influence the junction properties because it has a bandgap of 2.4–3.2 eV and n-type conductivity.^[30–33]

Summary of material analysis: 1) We find OVC in the Cu-poor CISe reference samples. This OVC is not seen in the treated samples. 2) The as-deposited CIS layers are uniform, and after sputtering, there is no evidence of reaction with the underlying CISe

layer. 3) We observe a higher SSSe ratio after annealing with Se + S than with Se in agreement with the additional S supply from the Se + S atmosphere.

3.2. Properties of CuInSe₂ Devices

The selenized and Se + S-treated CISe/CIS absorber microstructure and elemental distribution were investigated in the previous sections. The results were discussed in detail and compared with the nontreated samples as well as with the corresponding CISe references. From cut-out pieces of the same samples, solar cells were made and electrical characterization was conducted. In this section, the results from J–V and EQE measurements are summarized and discussed.

3.2.1. Solar Cell Performance

The measured electrical characterization (J–V and EQE curves) for the cells with the highest V_{OC} values and statistical variations of the device parameters (based on the analysis of 15 cells) are pictured in Figure 6 and 7, respectively. Secondary device parameters (i.e., ideality factor (n), saturation current density (J_0), and shunt resistance (R_{SH})) were extracted using the method described in.^[34] The obtained values and the corresponding discussion are provided in the body and the supporting text of Table S1, Supporting Information.

Regardless of composition, the reference and untreated samples to the post-treated samples with elemental Se and Se + S, show similar trends for the J–V curves in Figure 6a–c. The untreated CISe/CIS bilayers have very poor solar cell performance. Probably due to the blocking characteristics of the sputtered CIS layer, the collection probability of the minority carriers is extremely suppressed (wavelength independently), resulting in a very low J_{SC} . However, EQE analysis indicates that the reduced

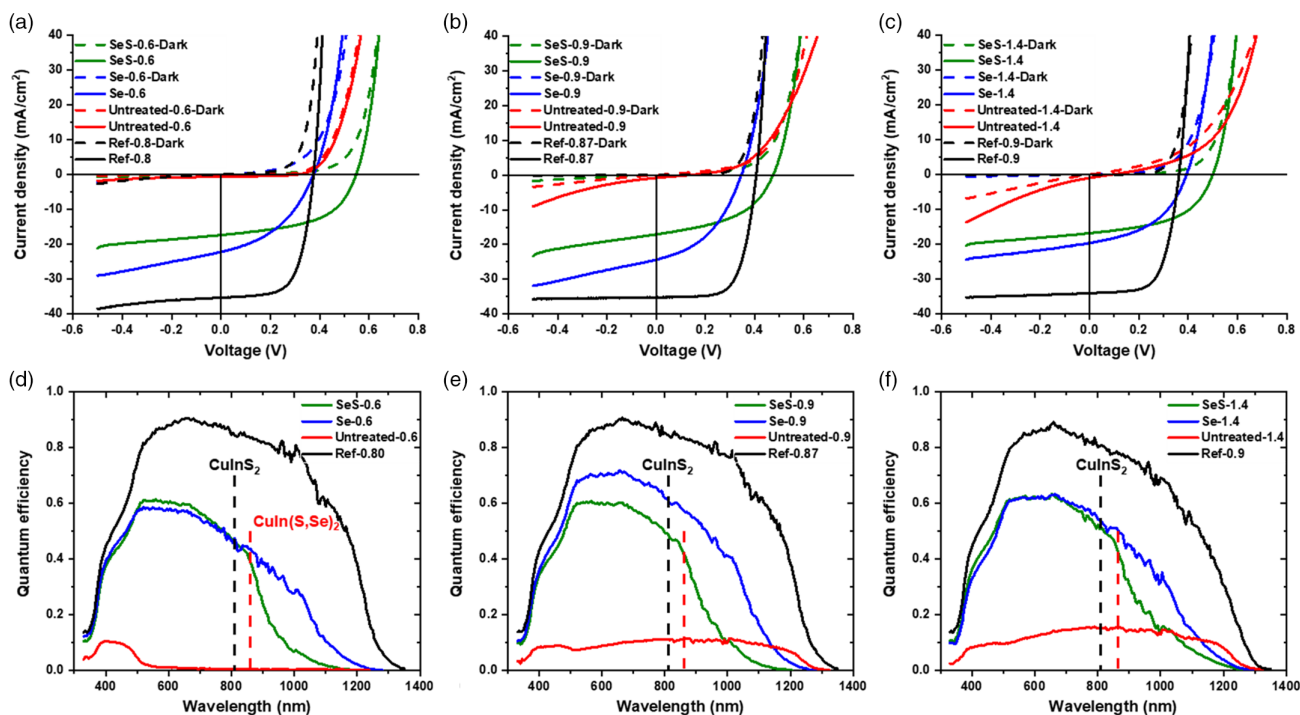


Figure 6. J - V (top row) and EQE (bottom row) of champion cells (selected with the highest V_{OC} values) obtained from the samples with a $[Cu]/[In]$ ratio in the top CIS layer equal to a,d) 0.6, b,e) 0.9, and c,f) 1.4. The dashed and solid lines in (a–c) represent the dark and light J - V , respectively. The reference bandgap values of $CuInS_2$ and $CuIn(S,Se)_2$ (with $SSe = 0.8$) are indicated by the dashed lines in (d–f) as a guide to the eye.

carrier collection is more severe for the untreated-0.6 sample than for the untreated-0.9 and untreated-1.4 (near-stoichiometric and Cu-rich) samples. Another explanation for the very low V_{OC} and J_{SC} may be a very high defect density in the nanograin top-layer and/or at its interface with $CuInS_2$ (potentially induced by the sputtering process). This points to a barrier at the Cu–In–S/ $CuInS_2$ interface being equally or more detrimental than the forming barrier after annealing (see the next paragraphs).

Samples Treated in Se: After the treatment in Se, the V_{OC} values are higher and comparable to the CISe reference cells. The EQE analysis shows that the optical bandgap of the cells is higher after selenization compared with the corresponding reference cells. The bandgap energies were determined from the EQE measurements applying a linear extrapolation at x -intercept of $[E \cdot \ln(1 - EQE)]^2$ versus E (photon energy), as illustrated in Figure 8. The optical bandgap is increased from $E_g = 1.00$ eV of the CISe samples to about 1.14 eV for the bilayer selenized samples, independently of the $[Cu]/[In]$ value in the top layer. The EQE results are consistent with the collection of carriers mainly from the high bandgap layer close to the surface with a small tailing in EQE originating from few electrons making it across the barrier at the $CuInS_2/CuIn(S,Se)_2$ interface.

Samples Treated in Se + S: For the sulfurized samples (Se + S), the maximum V_{OC} is measured for the SeS-0.6 sample, with a value of about 150 mV higher as compared with the CISe reference and selenized samples. However, the higher V_{OC} of this sample does not lead to the highest efficiency, because the EQE is significantly lower. The reason can be the blocking characteristic of the newly formed surface layer after recrystallization of the nanocrystalline CIS layer, which was also observed with

STEM (see Figure 5). Indeed, the extracted thickness (about 300 nm) of this layer and its high SSe ($[S]/[S] + [Se] = 0.8$) value at the surface are leading to a low carrier collection for this wavelength (>861 nm). For the top layer with $SSe = 0.8$, a bandgap ≈ 1.4 eV is expected which is in good agreement with the EQE results (see Figure 6d–f). Moreover, the analysis of the diode parameters strongly indicates an increasing voltage dependency of the current collection with increasing S incorporation, which is in line with the proposed formation of a transport barrier. Therefore, the expected cell improvement from a small to moderate widening of the surface bandgap was not obtained. The J - V does not show any effect on series resistance (R_s) or a back contact barrier, although the Cu in-diffusion (≈ 5 at% at the $Mo(S,Se)_2$ layer) along with S reaction may change the contact properties (see Figure 5). Furthermore, as confirmed by SEM (see Figure S1, Supporting Information), voids are formed for all the compositions. However, the impact of voids on cell results (J - V characteristics) is not completely understood. The impact of CA-CIS inclusion on the CIS absorber quality is also disputed. Some reports claim that the coexistence of CH and CA structure (nanoscale domains) in pure $CuInS_2$ films reduces the absorber quality (high intrinsic defects density^[35]), which leads to higher recombination and reduces the performance of solar cell devices.^[36–39] In contrast to the reported results of reduced performance, cell improvement was reported in the presence of a relatively small amount of CA-CIS phase^[40] in the absorber layer, similar to other secondary phases for other chalcopyrites.^[41,42]

For the treated samples with Se and Se + S, one could speculate that preserving high J_{SC} while increasing V_{OC} may be reached by applying lower annealing temperature, and/or

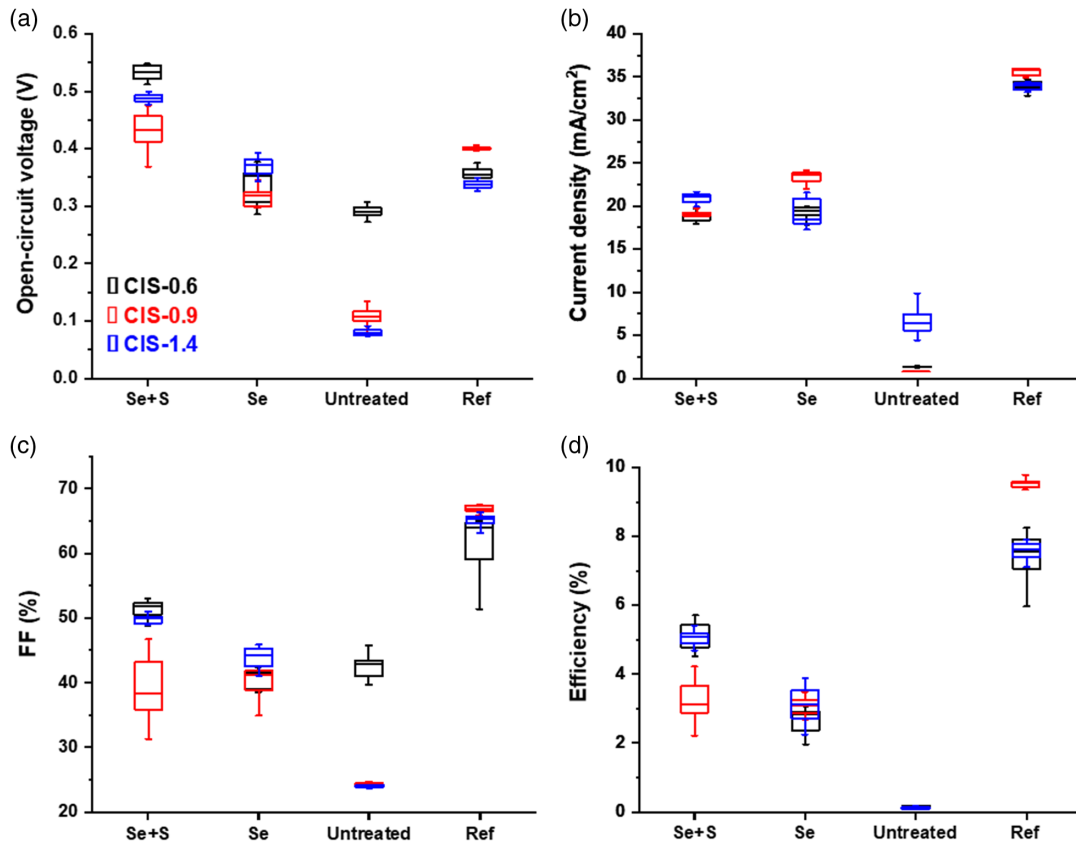


Figure 7. Statistical box charts of a) V_{OC} (mV), b) J_{sc} (mA cm^{-2}), c) FF (%), and d) Efficiency (%) for the references, the untreated and the annealed CISe/CIS.

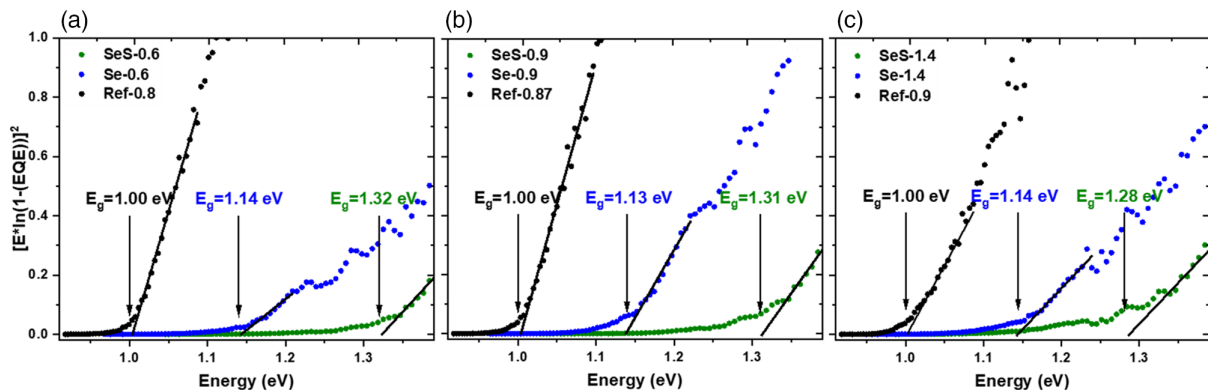


Figure 8. Plots of the $[E \cdot \ln(1 - \text{EQE})]^2$ versus photon energy for EQE curves presented in Figure 6. The bandgaps are determined as linear extrapolations at the x intercepts. For the untreated sample (CISe/CIS), the bandgap is not extracted by this method because of the too low carrier collection.

reducing the thickness of the top sputtered CIS layer with the aim of lowering the final SSSe. A pronounced recombination at the buffer/absorber interface after S incorporation is unlikely, since based on the first-principles calculations by others,^[43,44] and with considering the extracted SSSe values from the surface of the Se- and Se + S-treated samples (about 0.4 and 0.8, respectively), a detrimental cliff-like configuration is very unlikely, especially for the former sample. Another important parameter,

which could have an influence on the solar cell quality and performance of the devices is the Na content. The Na concentration of the investigated samples is evaluated in two regions of the GDOES depth profile (see Figure S11, Supporting Information): 1) in the absorber (surface) and 2) at the Mo/absorber interface, applying an area integration method. At the surface region of the absorber layers, the Na concentration for the treated samples is significantly higher than for the

reference and for the untreated samples, independently of [Cu]/[In] of the top CIS layer. However, due to the sample preparation prior to the XPS measurement, no evidence of Na was observed in the XPS overview spectra at 1071 eV (see Figure S3, Supporting Information). Therefore, further investigation is required to find a general statement or draw a conclusion regarding the possible correlation between Na and S concentration, and consequently, the formation of a possible NaInS₂ ternary phase. Finally, our samples were capped with CdS and etched several times during the processing. This capping process served successfully to suppress oxidation of the surface, but may have had adverse effects on the junction quality and thereby device performance.

Summary of device analysis: 1) We observe similar trends for the *J*-*V* and EQE curves of the treated samples, regardless of the composition ([Cu]/[In]) of the top-sputtered CIS layer. 2) After annealing with Se (or Se + S), about 140 meV (or 300 meV) higher optical bandgap (*E*_g) is observed for all the bilayers with different top layer compositions (Cu-poor, Cu-stoichiometric, and Cu-rich). 3) We observe a higher *V*_{oc} for the samples annealed in Se + S than for Se in agreement with a higher surface S composition. 4) We observe voltage-dependent current collection for all treated samples, but more pronounced for the sample treated in Se + S.

4. Conclusion

Bilayer samples with a coevaporated CuInSe₂ layer and a nanocrystalline-sputtered CIS precursor layer were prepared and annealed either in pure selenium or in sulfur + selenium atmosphere at a temperature of 530 °C. The samples before and after annealing as well as references with pure CuInSe₂ were analyzed using X-ray-based analyses, Raman spectroscopy, and compositional profiling techniques complemented by TEM. The results show that the approach of adding matrix elements together with sulfur followed by an anneal in only selenium leads to a more uniform depth distribution of sulfur and reduces long-range transport of copper than in earlier works when CISe single layers were annealed in a sulfur atmosphere. Raman and XRD analyses suggest that CISSe phases are formed close to the surface, while TEM shows reorganization of parts of the film down to the back contact, indicating that the anneal was too aggressive. Solar cell devices were fabricated, and EQE analysis demonstrated an absorption edge shift in agreement with an increased bandgap for the sulfur-containing devices as expected. We suggest a reaction route, where the nanocrystalline CIS layer is gradually consumed while supplying S (and Cu) into the underlying CISe layer and the excess In is being reacted with chalcogens from the atmosphere. Based on the material characterization, we conclude that our novel approach for sulfurization of CISe without the use of hazardous H₂S or H₂Se is promising, but the process needs further optimization to improve the solar cell efficiency.

Supporting Information

Supporting Information is available from the Wiley Online Library or from the author.

Acknowledgements

The Swedish Foundation for Strategic Research (SSF) provided support for this work under project number RMA15-0030. In addition, the authors acknowledge L. Riekehr for carrying out STEM-EDS analysis and all the colleagues in the solar cell division at the Ångström laboratory for their valuable contributions and help.

Conflict of Interest

The authors declare no conflict of interest.

Data Availability Statement

The data that support the findings of this study are available from the corresponding author upon reasonable request.

Keywords

CuIn(S,Se)₂ alloys, CuIn₅S₈, CuInS₂, CuInSe₂, gradient formation, sulfurization

Received: July 7, 2021

Revised: November 15, 2021

Published online: January 6, 2022

- [1] T. Kobayashi, H. Yamaguchi, Z. J. L. Kao, H. Sugimoto, T. Kato, H. Hakuma, T. Nakada, *Prog. Photovolt. Res. Appl.* **2015**, 23, 1367.
- [2] T. Maeda, R. Nakanishi, M. Yanagita, T. Wada, *Jpn. J. Appl. Phys.* **2020**, 59, SGGF12.
- [3] M. Marudachalam, H. Hichri, R. Klenk, R. W. Birkmire, W. N. Shafarman, J. M. Schultz, *Appl. Phys. Lett.* **1995**, 67, 3978.
- [4] S. Niki, M. Contreras, I. Repins, M. Powalla, K. Kushiya, S. Ishizuka, K. Matsubara, *Prog. Photovolt. Res. Appl.* **2010**, 18, 453.
- [5] J. Keller, O. V. Bilousov, E. Wallin, O. Lundberg, J. Neerken, S. Heise, L. Riekehr, M. Edoff, C. Platzer-Björkman, *Phys. Status Solidi A* **2019**, 216, 1900472.
- [6] U. Rau, M. Schmitt, F. Engelhardt, O. Seifert, J. Parisi, W. Riedl, J. Rimmach, F. Karg, *Solid State Commun.* **1998**, 107, 59.
- [7] V. Probst, W. Stetter, W. Riedl, H. Vogt, M. Wendl, H. Calwer, S. Zweigart, K.-D. Ufert, B. Freienstein, H. Cerva, F. H. Karg, *Thin Solid Films* **2001**, 387, 262.
- [8] M. Beres, K. M. Yu, J. Syzdek, S. S. Mao, *Thin Solid Films* **2016**, 608, 50.
- [9] *Solar Frontier press release*, http://www.solar-frontier.com/eng/news/2019/0117_press.html (accessed: May 2019).
- [10] D. Ohashi, T. Nakada, A. Kunioka, *Sol. Energy Mater. Sol. Cells* **2001**, 67, 261.
- [11] G. Wang, G. Cheng, B. Hu, X. Wang, S. Wan, S. Wu, Z. Dua, *J. Mater. Res.* **2010**, 25, 2426.
- [12] B. J. Mueller, M. Mock, V. Haug, F. Hergert, T. Koehler, S. Zweigart, U. Herr, *Thin Solid Films* **2015**, 582, 284.
- [13] J. K. Larsen, J. Keller, O. Lundberg, T. Jarmar, L. Riekehr, J. Scragg, C. Platzer-Björkman, *IEEE J. Photovoltaics* **2018**, 8, 604.
- [14] J. Keller, O. V. Bilousov, J. Neerken, E. Wallin, N. M. Martin, L. Riekehr, M. Edoff, C. Platzer-Björkman, *Solar RRL* **2020**, 4, 2000248.
- [15] F. Khavari, J. Keller, J. K. Larsen, K. V. Sopiha, T. Törndahl, M. Edoff, *Phys. Status Solidi A* **2020**, 217, 2000415.

- [16] H. Aboulfadl, J. Keller, J. Larsen, M. Thuvander, L. Riekehr, M. Edoff, C. Platzer-Björkman, *Microsc. Microanal.* **2019**, 25, 532.
- [17] M. Ishii, K. Shibata, H. Nozaki, *J. Solid State Chem.* **1993**, 105, 504.
- [18] G. B. Sakr, I. S. Yahia, M. Fadel, S. S. Fouad, N. Romčević, *J. Alloys Compd.* **2010**, 507, 557.
- [19] C.-H. Tsai, D. K. Mishra, C.-Y. Su, J.-M. Ting, *Int. J. Energy Res.* **2014**, 38, 418.
- [20] B. Asenjo, C. Guillén, A. M. Chaparro, E. Saucedo, V. Bermudez, D. Lincot, J. Herrero, M. T. Gutiérrez, *J. Phys. Chem. Solids* **2010**, 71, 1629.
- [21] S. Lugo, Y. Sánchez, M. Neuschitzer, H. Xie, C. Insignares-Cuello, V. Izquierdo-Roca, Y. Peña, E. Saucedo, *Thin Solid Films* **2015**, 582, 74.
- [22] R. Bacewicz, W. Gebicki, J. Filipowicz, *J. Phys.: Condens. Matter* **1994**, 6, L777.
- [23] J. Weszka, P. Daniel, A. Burian, A. M. Burian, A. T. Nguyen, *J. Non-Cryst. Solids* **2000**, 265, 98.
- [24] J. Álvarez-García, B. Barcones, A. Pérez-Rodríguez, A. Romano-Rodríguez, J. R. Morante, A. Janotti, S.-H. Wei, R. Scheer, *Phys. Rev. B* **2005**, 71, 054303.
- [25] D. S. Su, S.-H. Wei, *Appl. Phys. Lett.* **1999**, 74, 2483.
- [26] J. Álvarez-García, A. Pérez-Rodríguez, A. Romano-Rodríguez, T. Jawhari, J. R. Morante, R. Scheer, W. Calvet, *Thin Solid Films* **2001**, 387, 216.
- [27] J. Guillemales, P. Cowache, A. Lusson, K. Fezzaa, F. Boisivon, J. Vedel, D. Lincot, *J. Appl. Phys.* **1996**, 79, 7293.
- [28] T. Wada, N. Kohara, S. Nishiwaki, T. Negami, *Thin Solid Films* **2001**, 387, 118.
- [29] C. Stephan, *Dissertation, Structural Trends in off Stoichiometric Chalcopyrite Type Compound Semiconductors*, Freie Universität Berlin, **2011**.
- [30] K. Fukuzaki, S. Kohiki, S. Matsushima, M. Oku, T. Hideshima, T. Watanabe, S. Takahashia, H. Shimooka, *J. Mater. Chem.* **2000**, 10, 779.
- [31] A. Kudo, A. Nagane, I. Tsuji, H. Kato, *Chem. Lett.* **2002**, 31, 882.
- [32] P. Hu, C. K. Ngaw, Y. Y. Tay, S. Cao, J. Barber, T. T. Y. Tan, S. C. J. Loo, *Chem. Commun.* **2015**, 51, 9381.
- [33] N. Takahashi, H. Ito, A. Miura, N. C. Rosero-Navarro, Y. Goto, Y. Mizuguchi, C. Moriyoshi, Y. Kuroiwa, M. Nagao, S. Watauchi, I. Tanaka, K. Tadanaga, *J. Alloys Compd.* **2018**, 750, 409.
- [34] S. S. Hegedus, W. N. Shafarman, *Prog. Photovolt: Res. Appl.* **2004**, 12, 155.
- [35] D. Delmonte, F. Mezzadri, G. Spaggiari, S. Rampino, F. Pattini, D. Bersani, E. Gilioli, *Inorg. Chem.* **2020**, 59, 11670.
- [36] E. Rudigier, J. Alvarez-Garcia, I. Luck, J. Klaer, R. Scheer, *J. Phys. Chem. Solids* **2003**, 64, 1977.
- [37] E. Rudigier, I. Luck, R. Scheer, *Appl. Phys. Lett.* **2003**, 82, 4370.
- [38] J. Alvarez-García, E. Rudigier, N. Rega, B. Barcones, R. Scheer, A. Pérez-Rodríguez, A. Romano-Rodríguez, J. R. Morante, *Thin Solid Films* **2003**, 431–432, 122.
- [39] V. Izquierdo-Roca, X. Fontané, L. Calvo-Barrio, A. Pérez-Rodríguez, J. R. Morante, J. Álvarez-García, F. Duault, L. Parissi, V. Bermúdez, *Thin Solid Films* **2009**, 517, 2264.
- [40] A. Moreau, C. Insignares-Cuello, L. Escoubas, J.-J. Simon, V. Bermúdez, A. Pérez-Rodríguez, V. Izquierdo-Roca, C. M. Ruiza, *Sol. Energy Mater. Sol. Cells* **2015**, 139, 101.
- [41] C. Insignares-Cuello, C. Broussillou, V. Bermúdez, E. Saucedo, A. Pérez-Rodríguez, V. Izquierdo-Roca, *Appl. Phys. Lett.* **2014**, 105, 021905.
- [42] S. Theodoropoulou, D. Papadimitriou, A. G. Mamalis, D. E. Manolakos, R. Klenk, M.-C. Lux-Steiner, *Semicond. Sci. Technol.* **2007**, 22, 933.
- [43] O. Cojocaru-Mirédin, E. Ghorbani, M. Raghuwanshi, X. Jin, D. Pandav, J. Keutgen, R. Schneider, D. Gerthsen, K. Albe, R. Scheer, *Nano Energy* **2021**, 89, 106375.
- [44] E. Ghorbani, P. Erhart, K. Albe, *Phys. Rev. Mater.* **2019**, 3, 075401.
- [45] D. Papadimitriou, N. Esser, C. Xue, *Phys. Status Solidi B* **2005**, 242, 2633.